LANGMUIR
Article
pubs.acs.org/Langmuir

Hydrophobic Silica Nanoparticles Induce Gel Phases in Phospholipid Monolayers

Davide Orsi,[†] Tiziano Rimoldi,[†] Eduardo Guzmán,[‡] Libero Liggieri,[‡] Francesca Ravera,[‡] Beatrice Ruta,[§] and Luigi Cristofolini*,[†,‡]

[†]Dipartimento di Fisica e Scienze della Terra, Università degli Studi di Parma, Parma, Italy
[‡]Consiglio Nazionale delle Ricerche - Istituto per l'Energetica e le Interfasi, U.O.S. Genova (CNR IENI), Genova, Italy
[§]ESRF-The European Synchrotron, CS 40220, 38043 Grenoble, Cedex 9, France

Supporting Information

ABSTRACT: Silica nanoparticles (SiNP) can be incorporated in phospholipid layers to form hybrid organic–inorganic bidimensional mesostructures. Controlling the dynamics in these mesostructures paves the way to high-performance drug-delivery systems. Depending on the different hydrophobicity/hydrophilicity of SiNP, recent X-ray reflectivity experiments have demonstrated opposite structural effects. While these are reasonably well understood, less is known about the effects on the dynamics, which in turn determine molecular diffusivity and the possibility of drug release. In this work we characterize the dynamics of a mixed Langmuir layer made of phospholipid and *hydrophobic* SiNP. We combine X-ray photon correlation spectroscopy and epifluorescence discrete Fourier microscopy to cover more than 2 decades of *Q*-range (0.3–80 μm^{-1}). We obtain evidence for the onset of an arrested state characterized by intermittent stress-relaxation rearrangement events, corresponding to a gel dominated by attractive interactions. We compare this with our previous results from phospholipid/*hydrophilic* SiNP films, which show an arrested glassy phase of repulsive disks.

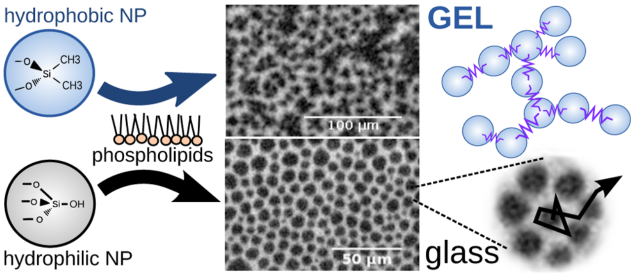

INTRODUCTION

Hybrid organic–inorganic nanostructures are promising as carriers for active ingredients, drugs, and chemicals. These systems have to face a wide range of external conditions; for instance, in the case of oral drugs to be absorbed at the intestine, the nanostructure has to resist pH variations from below 2 in the stomach to above 8 in the duodenum, to finally release its content in the intestine. Therefore, a smart system is required to protect, deliver and release their content on specific targets, avoiding its degradation during storage or undesired contact with not-target locations.[1,2] This complexity is tackled using multimaterial designs. The inorganic part may act as a scaffold—this is the case of mesoporous materials[3,4]—or may be embedded in organic emulsions and capsules to improve stability and to tune the releasability—this is the case for instance of hydrophilic nanoparticles helping the cell uptake of water insoluble drugs.[5]

SiNP with different hydrophilicity are used as adjuvants and/or stabilizing agents in drug-delivery systems: by altering the morphology and mechanical properties of membranes and liquid–liquid emulsions, they allow the fine-tuning of the release rate. For instance, drug-filled nanoemulsions adsorbed on hydrophobic SiNP (Aerosil R972) result in a gel-like paste formed by agglomerates: when placed in simulated gastric fluid, these protect the drug while releasing it gradually (20% in 2 h); in comparison, in the bare nanoemulsion the drug release is much faster (93% in 20 min).[6] Similarly, SiNP have been used to stabilize cubosomes of lyotropic lipids, systems with high drug solubility, both physically and against enzymatic digestion.[7,8] On the other hand, the addition of hydrophilic SiNP to drug-loaded lipid microparticles—made of mixtures of mono-, di-, and triglycerides of stearic and palmitic acids—doubles the 90 min release rate of drugs for respiratory diseases such as asthma,[9] favoring their water solubility. Furthermore, the different degrees of hydrophilicity/hydrophobicity of silica nanoparticles (SiNP) set where the nanoparticles localize within membranes:[10,11] hydrophilic SiNP are physically adsorbed at the membrane surface, while hydrophobic SiNP are incorporated into the lipophilic inner part of the membrane. In fact, X-ray reflectivity experiments showed that SiNP alter the lamellar to inverted hexagonal phase transition of phospholipid layers, with hydrophobic particles favoring the hexagonal phase while hydrophilic ones stabilize the lamellar phase.[12]

While structural and morphological effects are relatively well-understood, much less evidence is available about the effects of SiNP incorporation on the internal dynamics of the membranes, which in turn determines molecular diffusivity

Received: March 2, 2016
Revised: April 28, 2016
Published: May 2, 2016

DOI: 10.1021/acs.langmuir.6b00813

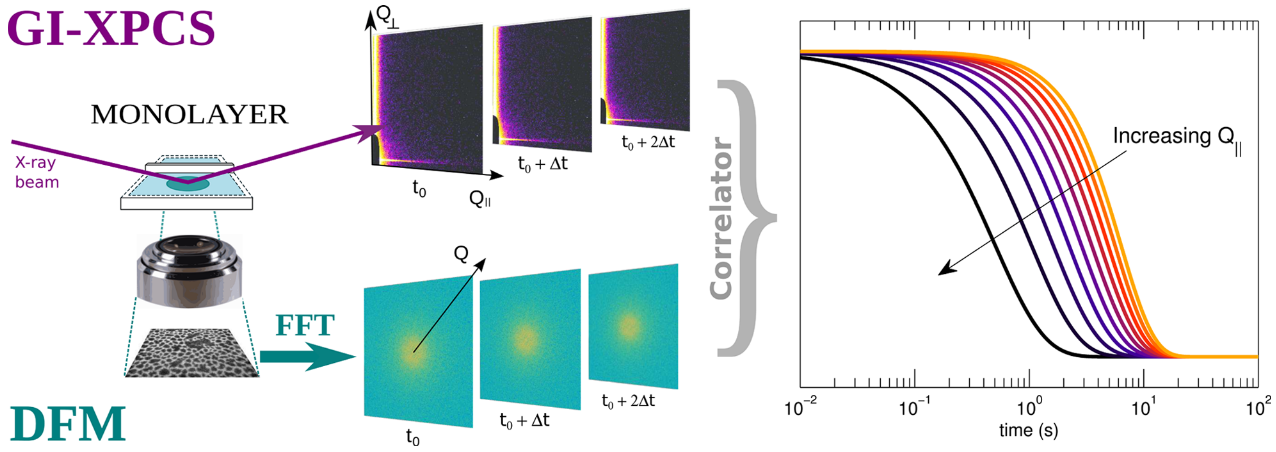

Figure 1. X-ray photon correlation spectroscopy and epifluorescence discrete Fourier microscopy allow the characterization of the microscopic dynamics of 2D layers; their combination effectively extends the *Q*-range explored beyond the limits of each technique.

and drug release rates. This because most of the experimental approaches so far were not focused on the microscopic characterization of the dynamics down to the nanoscale. Recently, we demonstrated that this is feasible using an experimental approach that combines scattering and fluorescent microscopy techniques.[13] By combining epifluorescence microscopy tracking and discrete Fourier microscopy (DFM), a technique that analyzes the temporal evolution of microscopy images in Fourier space, with grazing incidence X-ray photon correlation spectroscopy (GI-XPCS), the analogue of dynamic light scattering using X-ray in grazing incidence geometry, we have been able to characterize a transition from Brownian to arrested dynamics in a mixed Langmuir monolayer of phospholipids and hydrophilic SiNPs.

In this work, we combine GI-XPCS and epifluorescence DFM to investigate a mixed Langmuir monolayer of 1,2-dipalmitoyl-*sn*-glycerol-3-phosphocholine (DPPC) and hydrophobic SiNPs; a sketch of the experimental approach used is reported in Figure 1. We choose DPPC as it is the prevalent component of lung surfactants as well as of many cellular membranes. We focus here on the effects of SiNPs on the morphology arrangements and nanoscopic dynamics at different values of film compression, and we characterize the arrest transition as that of an attractive gel.

■ MATERIALS AND METHODS

Materials. DPPC was purchased from Sigma (Germany) at 99% purity and used without further purification. The molecular weight of this lipid is 734.1 g/mol. Solutions of lipids for the spreading were prepared using 99.9% pure chloroform from Sigma (Germany). Hydrophobic fumed silica nanoparticles (SiNP) employed in this work are Aerosil R972 purchased from Evonik-Degussa (Germany). They are produced by the continuous flame hydrolysis processing of SiCl4, resulting in sintered clusters of spherical primary particles. In our case the primary particles are composed by amorphous silica, pure at 99.8%, with density 2.4 g/cm^3, average size of 16 ± 3 nm, and Brunauer−Emmett−Teller (BET) specific surface area of 110 m^2/g. According to the information on the producer, their hydrophobic character is obtained by a specific treatment with dimethylchlorosilane made at the final stage of the production process. This results in irreversible attachment of methyl groups at the particle surface. The SiNP thus produced are free from any surface-active contaminant. In fact, the surface tension of a pristine SiNP Langmuir layer is not appreciably different from that of pure water, unless the particle layer is highly packed.

For the spreading, a chloroform solution of DPPC and a chloroform suspension of SiNP with equal mass concentrations are prepared and mixed in 1:1 proportions. This mixture is spread at the air/water interface using a Hamilton syringe to obtain a 1:1 DPPC−SiNP Langmuir film with initial surface concentration Γ = 1.8 mg/m^2. For epifluorescence investigation, 16:0−12:0 nitrobenzoxadiazole−phosphatidylcholine (NBD-PC) from Avanti Polar Lipids (CAS: 105539-26-2) was added in the concentration 1% to the lipid.

Epifluorescence Microscopy. Epifluorescence images have been recorded using a Nikon Eclipse Ti inverted microscope equipped with a custom-made Langmuir trough. The trough has a quartz window in its center to grant optical access; a Nima Wilhelmy balance is used to measure the surface pressure; the equipment operates using Riegler & Kirstein's electronics. A 20× objective with ultralong working distance was used; images were recorded using an Andor Clara camera, for a pixel size of 1 pixel = 0.946 μm.

Grazing Incidence X-ray Photon Correlation Spectroscopy. GI-XPCS experiments were performed at the beamline ID10 of the European Synchrotron Radiation Facility (ESRF) in Grenoble, France. An incident X-ray beam with an energy of 8 keV and λ = 0.155 nm was selected from the undulator radiation by a water-cooled Si(111) pseudochannel cut monochromator scattering in vertical geometry (energy bandwidth $\Delta E/E \sim 10^{-4}$). The beam was then focused with Be compound lenses while higher harmonics were suppressed by a white beam double mirror placed before the main monochromator. The spatially coherent part of the incoming radiation was selected by using roller-blade slits opened to 10 × 10 μm, placed ~0.18 m upstream of the sample. The parasitic scattering produced by the beam-defining slits was removed by carefully adjusting a set of guard slits a few centimeters upstream of the sample. The resulting incident flux on the sample was 3×10^{10} photons/s/100 mA. The beam was reflected to impinge on the liquid surface at a grazing incident angle of 0.12°, which is about 90% of the critical angle for total reflection on the water surface at this photon energy.

A custom-made Langmuir trough with a single moving barrier (maximum surface 418 × 170 mm^2) was installed on the sample diffractometer. The trough was mounted on an active antivibration table; it was equipped with a plastic enclosure under which a helium atmosphere was created, in order to minimize parasitic scattering from air and to reduce risks of beam-induced damage. A KSV-Nima Wilhelmy balance and electronics were used to control the trough and measure the surface pressure Π and the trough's area during GI-XPCS measurements.

Two-dimensional X-ray scattering speckle patterns were recorder using a Medipix photon counting area detector,[14] made of 256 × 256 pixels, each 55 μm in size. The detector was placed at a distance of 3.38 m from the sample. The exposure time has been chosen to be long enough to warrant a reasonable S/N ratio, 5−20 ms in our case. A shutter, synchronized with the area detector, was placed upstream of the sample to turn off the beam between measurements. Image sets up to 10 000 images were collected for different surface concentrations, with different exposure times. The pixels of the 2D detector have been divided into groups, each of which is labeled by the averaged values of scattering vector components in the directions parallel ($Q_{\|}$) and perpendicular ($Q_{\perp}$) to the air/water interface. We calculate by software the autocorrelation function of the scattered intensity $I(t)$ measured by each group of pixels as

$$g^{(2)}(Q_{\|}, Q_{\perp}; t) = \frac{\langle I(t_0) I(t_0 + t)\rangle_{t_0}}{\langle I(t_0)\rangle_{t_0}^{\ 2}} \tag{1}$$

Discrete Fourier Microscopy. The dynamics of the systems in momentum space can be measured using microscopy through the temporal autocorrelation of Fourier transforms of epifluorescence videos, a technique named discrete Fourier microscopy (DFM).[15] Using the epifluorescence microscopy setup, we measured videos at 5−10 frames/s in correspondence of specific values of surface pressure. The barriers of the Langmuir trough were blocked during measurements. A steel ring of 1 cm diameter has been placed along the light path, submerged in the water subphase. Its thickness was slightly lower than the water subphase's height: this effectively reduced collective drifts of the film by suppressing convective motions in the water bulk. Any remaining collective drift of the film was corrected by template alignment of a region of interest of a portion of the images, using the ImageJ software.[16] We converted each sequence of images to a sequence of binary images by applying a threshold that marks as 1 the pixels of the liquid-compressed (LC) domains and 0 elsewhere. Then, we calculated the 2D fast Fourier transform power spectrum of each binary frames. The power spectrum was shifted to have zero frequency in its center, and then its pixels have been grouped into concentric rings, each labeled by the pixels' average value of Q. Using eq 1, we calculate by software the intensity autocorrelation function of the intensity of each ring of pixels of the FFT spectrum as a function of time.

■ RESULTS AND DISCUSSION

Morphology of the Film. Epifluorescence microscopy characterizes the morphology of the DPPC−SiNP film by monitoring a small fraction of molecules labeled with a fluorescent dye, which are confined upon compression in the liquid expanded (LE) phase of a Langmuir monolayer.[17,18] In Figure 2e, we report the surface pressure Π as a function of the surface density Γ of the mixed layer. As Π increases from $\Pi \simeq 0$, small liquid-condensed (LC) domains appear, as shown in Figures 2a,b. The size of LC domains rapidly grows; at $\Pi \geq 4$ mN/m both their size and their morphology reach some saturation value. Figures 2b,c show the high size polydispersity and the very diverse shapes of LC domains; actually, larger domains appear to be clusters of smaller domains with a more regular shape. At further compression, the packing fraction of LC domains increases linearly. More details on this linear growth are reported as Supporting Information (Figure S1). Finally, at $\Gamma > 6.3$ mg/m^2 ($\Pi > 20$ mN/m) a denser phase of reticular structures is formed, which we term dense gel (Figure 2d); the mixed DPPC−SiNP phase, i.e. the light areas of the image, is now reduced to a thin network that separates darker domains. The transition to this phase is highlighted by a steeper increase of $\Pi(\Gamma)$ (Figure 2e); in this regime, the packing fraction of domains does not increase upon further compression.

Similar reticular gel structures were observed in Langmuir films made of hydrophobic gold nanoparticles.[19] In that case, hydrophobic coating induces particle aggregation into clusters located at the air/water interface. When the size of these clusters reaches the micron range, individual clusters aggregate forming string-like objects because of water meniscus mediated interactions. Upon compression, these strings are connected, forming a reticular network. Its mechanical response is that of a gel.[20] A similar aggregation mechanism—probably complicated by the interaction with DPPC molecules—might explain also the phenomenology observed in our system.

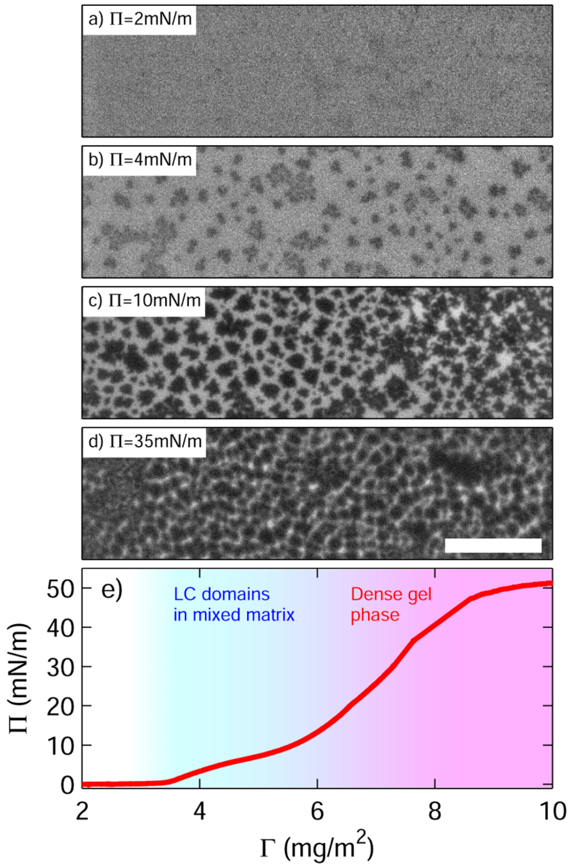

Figure 2. The presence of nanoparticles causes the formation of clusters of liquid-condensed phospholipid domains, at the same time preventing coalescence. (a−d) Epifluorescence images measured at increasing values of surface pressure Π; all pictures have the same size and magnification; the white bar is 150 μm long. (e) The surface pressure Π grows as the surface density Γ is increased. Above the gas phase where Π is zero, two regions can be identified. For 3.5 mg/m^2 < Γ < 6.3 mg/m^2 we observe coexistence of LC DPPC domains in a mixed DPPC−SiNP phase (blue). At $\Gamma > 6.3$ mg/m^2 we observe a denser phase of reticular structures that we term dense gel, and the $\Pi(\Gamma)$ trend becomes steeper (red).

In this respect, the gel phase found in our system is different from that found in 3D multilamellar organizations of amphiphilic molecules,[21] where the gel-like character of the system is linked to the arrangement and ordering of polar heads and hydrophobic tails between different layers. In our system, the properties of the 2D gel phase formed by the self-organization of phospholipids and SiNP are connected to their *lateral* arrangement. Both the formation process and the morphology of this gel phase have strong resemblances to the gels obtained by diffusion-limited cluster aggregation at interfaces (DLCA).[22]

Microscopic Dynamics. By GI-XPCS and DFM we obtain Q-dependent intensity signals respectively as scattered X-ray intensity recorded in grazing-incidence small-angle geometry (GI-SAXS) and power spectrum of the Fourier transform of epifluorescence microscopic imaging (DFM). In both cases, we

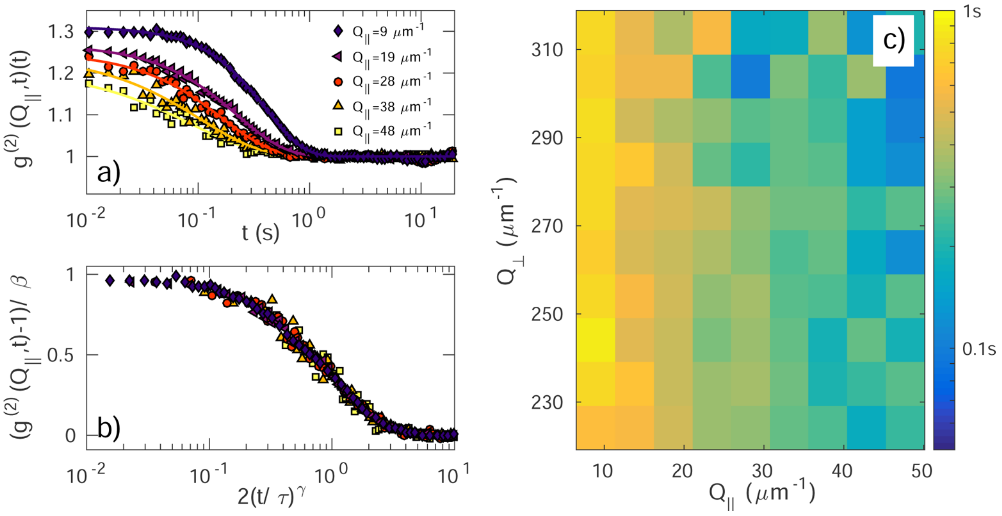

Figure 3. GI-XPCS correlation functions decay following the Kohlrausch−Williams−Watts (KWW) law. The dynamics are confined at the air/water interface. (a) Correlation functions measured at Π = 12 mN/m and at different values of $Q_{||}$. Lines are fit with eq 2 (KWW law). (b) The same correlation functions, normalized by the contrast and reported on the rescaled axis $2(t/\tau)^{\gamma}$, collapse on a single curve. (c) τ_{eff} obtained by the fits is reported as a color map as a function of $Q = (Q_{||}, Q_{\perp})$; it depends only on the component parallel to the interface $Q_{||}$.

calculate the temporal autocorrelation of this signal in the form of $g^{(2)}(Q;t)$.[23] Its decay is well described by a Kohlrausch−Williams−Watts (KWW) modified exponential

$$g^{(2)}(Q_{||};\ t) = A + \beta e^{-2(t/\tau)^{\gamma}} \tag{2}$$

Here, τ is the relaxation time of the dynamics and β is the contrast; the parameter γ sets the shape of the exponential curve, indicating whether $g^{(2)}$ decays faster ($\gamma > 1$, compressed shape) or slower ($\gamma < 1$, stretched shape) than a simple exponential. *A priori*, in a generic GI-XPCS experiment, the parameters τ, β, and γ could depend on both components of the scattering vector $(Q_{||}, Q_{\perp})$ parallel and perpendicular to the interface. The value of γ is linked to the dynamical regime that characterize the system, together with the dependence of τ from Q: in the case of Brownian dynamics, $\tau \propto Q^{-2}$ and $\gamma = 1$; pure ballistic motion shows $\tau \propto Q^{-1}$ and $\gamma = 2$.[24] More complex systems display an intermediate behavior that eludes these simplest models, e.g., in the case of polymeric layers or 2D gel networks in which the correlation functions have compressed exponential form[25,26] with characteristic time $\tau \sim Q^{-1}$, or in aged colloidal creams,[27] aged Laponite,[28,29] and methylcellulose[30] gels, systems where stretched exponential correlation functions are found with $\tau \sim Q^{-1}$. Here, we use the parameters obtained from fits to eq 2 to investigate the effects of a controlled increase of surface compression/surface pressure on the interfacial dynamics of the system. It is worth noting that while in DFM the scattering vector Q lies naturally in the plane parallel to the air/water interface, in GI-XPCS experiments we have to decompose Q in its components parallel and perpendicular to the interface, $Q_{||}$ and $Q_{\perp}$.

Figure 3a reports GI-XPCS correlation functions measured at Π = 12 mN/m for $Q_{\perp}$ = 270 μm^{-1} and increasing values of $Q_{||}$; experimental curves (filled symbols) have been fit with eq 2 (continuous lines). Both τ and Γ decrease with increasing $Q_{||}$. In Figure 3b, correlation functions are reported normalized by the contrast and on a rescaled time axis $2(t/\tau)^{\gamma}$; the data curves collapse on the same simple-exponential trend, confirming the goodness of the fit. In Figure 3c we report the relaxation time τ as a color map, as a function of the components of the scattering vector $(Q_{||}, Q_{\perp})$; the plot shows that the dynamics are confined at the air/water interface because τ depends only on $Q_{||}$. In all the successive analysis of data collected at increasing values of Π, the correlation functions have been calculated on groups of pixels that span the whole $Q_{\perp}$ range available, to improve the signal-to-noise ratio.

An analogous phenomenology is found in DFM correlation functions; Figure 4a reports raw correlation functions measured at Π = 10 mN/m. In Figure 4b they are normalized and reported on the rescaled axis $2(t/\tau)^{\gamma}$: again, they collapse on a single curve. Both GI-XPCS and DFM correlation functions show a decrease of contrast β for increasing values of Q. This decrease is termed pseudo-Debye−Waller and is linked to the

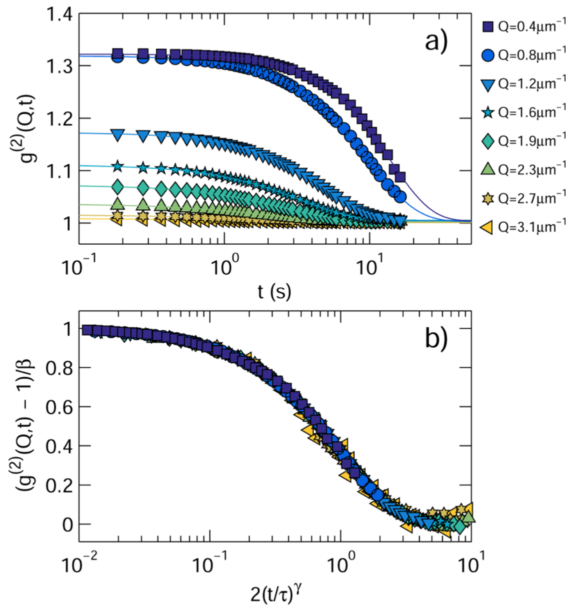

Figure 4. (a) DFM correlation functions measured at 10 mN/m and increasing values of Q. Lines are fits to eq 2. (b) The same correlation functions, when normalized, collapse on a single curve on the rescaled axis $2(t/\tau)^{\gamma}$.

DOI: 10.1021/acs.langmuir.6b00813
Langmuir 2016, 32, 4868−4876

presence of dynamics faster than the experimental integration time, as discussed in the Supporting Information and shown in Figure S2.

As stated at the beginning of this section, the particular relation between relaxation time and Q is connected to the kind of dynamics present in the sample. To take into account the changes in shape of the decay (as described by γ), we calculate an effective relaxation time, which is the first moment of $g^{(2)}$:

$$\tau_{\mathrm{eff}}(Q) = \frac{\tau(Q)}{\gamma(Q)}\Gamma\left(\frac{1}{\gamma(Q)}\right) \tag{3}$$

where Γ is the gamma function. In Figure 5, we report $\tau_{\mathrm{eff}}(Q)$ for several values of Π. The combined use of GI-XPCS and DFM allow us to cover more than 2 decades of Q-range and therefore to evaluate accurately the power law $\tau \propto Q^{-n}$. At low pressure we find $n = 1$ (trend represented as a dashed line in the figure), while n decreases when the pressure is increased, as shown in the inset. The limiting value observed at (e.g., $\Pi = 40$ mN/m) is $n = 0.7$ (dash-dotted line in the figure). We attribute the decrease of n to the onset of dynamical arrest, in analogy with the results found in 3D in an aging colloidal gel formed by PMMA particles and polystyrene dispersed in decalin.[31] In that case, the dominant dynamical process is the release of stresses, leading to $\tau \propto Q^{-0.5}$ and compressed exponential shape of the correlation functions.

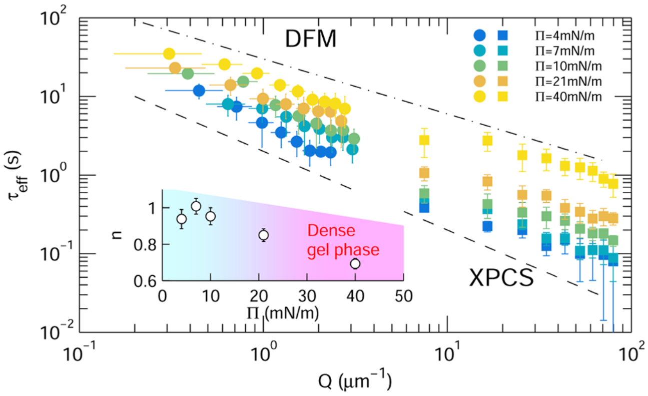

Figure 5. Effective relaxation times measured by GI-XPCS (squares) and DFM (circles) as a function of Q. The horizontal error bars indicate the Q-range over which τ is measured. Despite the large difference in the spatial scale investigated with the two techniques, the data fall along power law trends $\tau \propto Q_{\|}^{-n}$. We find $n \simeq 1$ (dashed line) at low Π. At higher values of Π, corresponding to the dense gel phase, we find a less steep dependence with $n = 0.7$ (dash-dotted line). The inset reports the power law exponent n as a function of Π.

In Figure 6 we report as a color-map the shape parameter γ (panel a) measured using GI-XPCS as a function of $Q_{\|}$ and Π. The behavior of γ as a function of $Q_{\|}$ and Π is intriguing. At surface pressure $\Pi \leq 7$ mN/m, we find $\gamma \sim 1$ decreasing slightly to $\gamma \sim 0.7$ at larger $Q_{\|}$. As Π increases, γ increases and its $Q_{\|}$ dependence becomes steeper, until saturation at value $\gamma \sim 1.7$ is reached at $\Pi \sim 40$ mN/m. Analogous results are found using DFM. In panel b we compare the rescaled time $\tau_{\mathrm{eff}}Q$ measured using GI-XPCS (at $Q_{\|} = 23$ μm^{-1}, filled circles) and using DFM (at $Q = 1$ μm^{-1}, empty circles) with the elastic modulus E_1 (squares) measured using the oscillating barriers technique.[32] Data are reported on superimposed semilogarithmic axis; both y-axes span 2 orders of magnitude. Both $\tau_{\mathrm{eff}}Q$ and E_1 increase with increasing values of Π for $\Pi < 30$ mN/m; as the compaction of the film is further increased, the dynamics of the system are slowed down and—correspondingly—the mechanical modulus of the film grows. It is worth noting that different measurements yields different results in the Π region corresponding to the high-Γ dense gel phase: the spreading of the data points measured with the different techniques is due to the breaking of the $\tau \propto Q^{-1}$ scaling of the relaxation times.

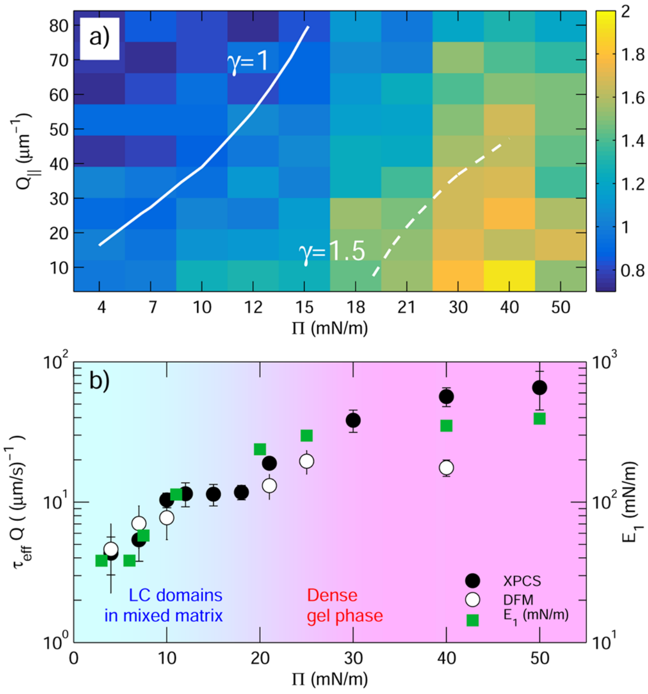

Figure 6. (a) Color map of the dependence of γ on $Q_{\|}$ and Π. The white lines indicates contours for $\gamma = 1$ (solid line) and $\gamma = 1.5$ (dashed) obtained from a smoothed color map, to act as guides to the eye; (b) rescaled time $\tau_{\mathrm{eff}}Q$ measured by GI-XPCS at $Q_{\|} = 23$ μm^{-1} (filled circles), $\tau_{\mathrm{eff}}Q$ measured by DFM at $Q = 1$ μm^{-1} (empty circles) and the elastic modulus E_1 (squares) are reported as a function of Π on semilogarithmic axis. The two logarithmic axes span equally sized ranges.

This phenomenology is not compatible neither with Brownian diffusion nor with Ballistic motion. In the first case, because the presence of simple or stretched exponential decays at low Π is not matched by a $\tau \propto Q^{-2}$ dependence of the relaxation time; for the latter, compressed exponential with $\gamma = 2$ has not been observed. On the contrary, the behavior of τ_{eff} and γ has a strict analogy to that found by GI-XPCS on a 2D gel of gold nanoparticles;[33] moreover, the evolution of the macroscopic elastic modulus was found to be the same as that of the characteristic relaxation time for that system as well.

In our system, the shape of the relaxation (Figure 6a), the Q-dependence of τ_{eff} (Figure 5a), and mostly the strict analogy between the evolution of the elastic modulus E_1 and the characteristic time τ_{eff} for the fluctuations (Figure 6b) all qualitatively agree with a model put forward long ago by Bouchaud and Pitard.[34] This model assumes the dynamics to be governed by microcollapses of the gel, resulting in the formation of force dipoles, which affect the surrounding particles by inducing a strain field. With the further assumptions that the collapses occur randomly in space and time, the stochastic equations of motion for the strain field can be solved analytically. An important parameter of the model is θ, the typical collapse time. In the slow-collapse regime, i.e., for times

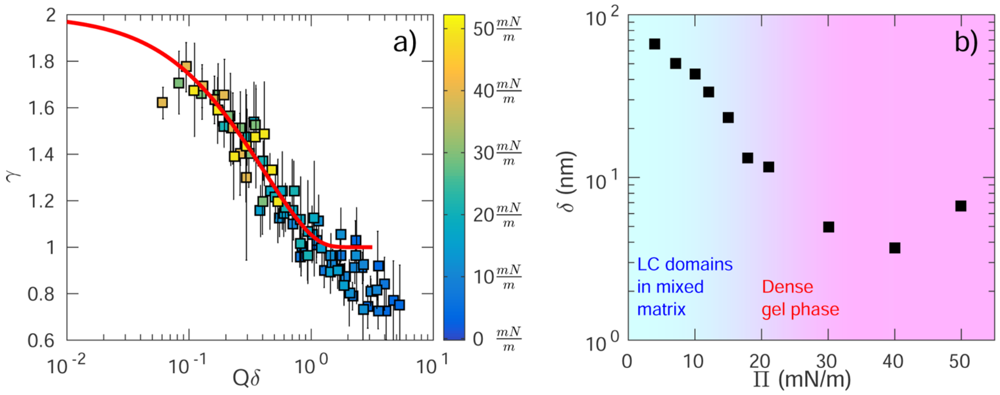

Figure 7. (a) Master curve built from $\gamma(Q)$ curves measured at different Π using GI-XPCS. $\gamma(Q_{\|})$ curves are shifted along the x-axis by the scaling length δ so that they overlap. The resulting master curve was built so that $\gamma < 1$ happens at $Q\delta \geq 1$, in agreement with the model.[35] The red line represents the prediction of the modified Duri−Cipelletti model described in the text. (b) Long-time displacement length δ as a function of Π. δ decreases steadily with increasing Π, reaching a limiting value of a few nanometers around $\Pi \simeq 30$ mN/m, i.e. in the red region, that marks the Π range corresponding to the dense gel phase.

shorter than θ, the resulting intermediate scattering function has a compressed shape with $\gamma = 1.5$, while the relaxation time is inversely proportional to the momentum Q and is proportional to the macroscopic elastic modulus of the gel. This detailed model, however, puts strict limits to the Q-dependent values assumed by γ and cannot account for the complex phenomenology summarized in Figure 6. In particular, only two regimes are possible whenever $\tau \propto Q^{-1}$, namely $\gamma = 1.5$ and $\gamma = 1.25$, thus excluding important parts of the plane in Figure 6.

On the contrary, the observed dynamics can be described in light of a model recently proposed by Duri and Cipelletti,[35] which postulates the presence of intermittent rearrangements taking place with average rate ν on a typical length δ (which is not the same length identified by the pseudo-Debye−Waller analysis reported in the Supporting Information). Each of these events causes a decrease of correlation in $g^{(2)}(Q;t)$ until total decorrelation is reached after a sufficiently high number of events have taken place. The probability distribution of events as a function of time is assumed to be Poissonian. The decrease of correlation $h(m,Q)$ due to m rearrangements is linked to the probability function of the displacement lengths ΔR observed in the gel, which is assumed to be Levy-like[35,36] with its tail toward large ΔR being proportional to ΔR^{-p} with $p = 2.5$. Under these assumptions, the model predict a transition from $\gamma = p - 1 = 1.5$ to $\gamma = 1$ as a function of Q. For $Q\delta > 1$ a single displacement is sufficient to fully decorrelate the signal, resulting in a simple exponential decay of the correlation function; the fact that we observe also stretched exponential decays with $\gamma < 1$ may be attributed to spatially heterogeneous distribution of relaxation processes generates a distribution of relaxation times. Our results show some discrepancies with the original Duri−Cipelletti model. This is true in particular for the behavior of γ, as shown in Figure 6b. We found $\gamma > 1.6$ at low q and high surface pressure while the model predicts $\gamma \leq 1.5$. This can be explained with a steeper decay of the displacements' probability distribution in the low-q and large Π regime, $\Delta R^{-(\gamma+1)}$, if compared with the Levy-like distribution originally assumed in the model.

To compare our results with the just described variant of the model proposed in ref 35, we report values of γ measured at each surface pressure in Figure 7a, on the adimensional axis $Q\delta$, varying δ so that they overlap collapsing on a master curve, in analogy with Figure 7 of ref 33. The pronounced ballistic character of the dynamics allows to build the red curve in Figure 7 on the assumption of a distribution of rearrangements whose tail is proportional to ΔR^{-3}. The ambiguity of the absolute scale of δ is solved by matching our choice of δ accordingly to the fact that for $Q\delta > 1$ the model predicts $\gamma = 1$. The master curve thus obtained is in agreement with the model curve up to $Q\delta = 2$, above which value the model would plainly predict $\gamma = 1$, while we observe a stretched shape that implies a spatially heterogeneous distribution of relaxation times. The scaling parameter δ is an estimate of the characteristic displacement length of the dynamics taking place on the time scale of τ; we report it as a function of Π in Figure 7b, on the semilogarithmic axis, for both GI-XPCS and DFM data. We find that the value decreases rapidly with increasing Π; δ decreases steadily with increasing Π, reaching a limiting value of a few nanometers around $\Pi \simeq 30$ mN/m. These results confirm that the dynamics of the system have been modified—upon compression—by the formation of a compact layer, where we already found a weak $\tau \propto Q^{-0.7}$ dependence. In this highly arrested state, the rearrangements of the film structure are confined on nanometric length scales.

Interestingly, DFM and GI-XPCS yields different values of δ; the values of δ measured by DFM follows the same trend of those of GI-XPCS, but they are 1 order of magnitude larger. We note that the values of δ measured using DFM fall below the resolution limit of the epifluorescence microscope; this might explain the inability of DFM to correctly measure the value of δ.

■ CONCLUSIONS

We find that the incorporation of hydrophobic silica nanoparticles in the DPPC monolayer results in the formation of a mixed DPPC-SiNP 2D gel, similar to the fractal 2D gel network formed by attractive microparticles.[37] The liquid-compressed domains surrounded by this mixed network have irregular shape, and they are—on average—smaller than those of pristine DPPC; larger domains are clusters of small domains. Upon compression, the size of the domains remains constant while their surface concentration increase, leading to the formation of a dense gel phase for surface pressure $\Pi > 20$ mN/m. On the contrary, hydrophilic silica was shown to induce a stabilization of the LC/LE phase coexistence, with LC domains surviving along the whole surface pressure/area isotherm.[13]

The microscopic dynamics are similar to that of a system characterized by attractive interactions; in this case, random intermittent rearrangements taking place on the submicron spatial scale[35] are deemed responsible for the observed dynamics. Upon compression, the characteristic length δ of these rearrangements continuously decreases, reaching a limiting values of a few nanometers for Π = 30 mN/m. We find that the relaxation time increases in the same fashion as the elastic macroscopic response to mechanical stress, a feature expected for a gel with microcollapses that induce a strain field that affects the dynamics of the system.[34,38] This indicates that the film is not completely arrested, even in its higher compaction state. In similar experiments with layer of gold nanoparticles at the air/water interface, interacting via attractive potentials, comparable results indicated the formation of a percolating network of nanoparticles.[33,39]

This dynamics is significantly different from that found for DPPC−hydrophilic SiNPs films, where the dynamics at low surface concentration is diffusive. Upon compression, we observed a transition to an arrested, cage-limited dynamical regime that we interpreted as due to repulsive interactions;[13] moreover, we identified a threshold value for the surface concentration of LC domains that marks the transition.

In Figure 8, we compare the effects of SiNP of different hydrophilicity through the analysis of the exponent n of the power law trend $\tau \propto Q^{-n}$ and of the shape exponent γ measured at $Q_{||}$ = 27 μm^{-1}. The same results are summarized also in Table 1.

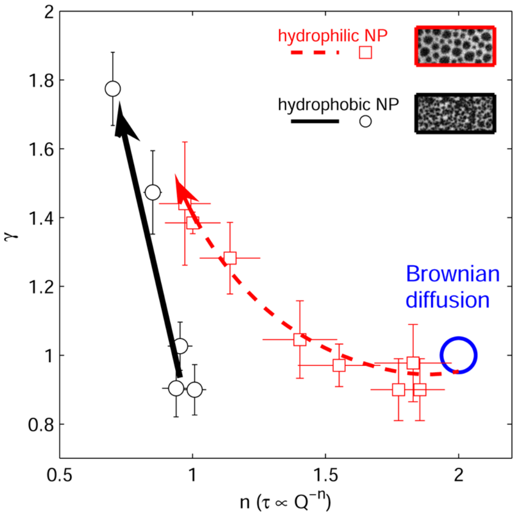

Figure 8. Comparison of the different dynamical regimes induced by hydrophobic and hydrophilic SiNP when added to DPPC monolayers. Data are reported on the plane identified by γ measured at $Q_{||}$ = 27 μm^{-1} and by the exponent n of the power law trend $\tau \propto Q^{-n}$. For hydrophobic SiNP, γ increases from 1 up to 1.8 while n decrease from $\simeq$1 to 0.7 (circles) upon compression (black arrow). In the case of hydrophilic SiNP a different region of the γ−n plane is explored; upon compression (red arrow) we observe a transition from Brownian diffusion (blue circle) to an arrested dynamics ruled by repulsive interaction[13] with γ = 1.5 and n = 1 (squares). The morphology corresponding to the two arrested states is shown in the legend.

Table 1. Comparison of Dynamical Regimes Found for Mixed DPPC−Nanoparticle Layers for SiNPs of Different Hydrophilicity, As Identified by $\gamma(Q)$ and by the Power Law Exponent n of the $\tau(Q)$ Dependence[a]

	hydrophilic SiNP	hydrophobic SiNP
low Γ	$\gamma \simeq 1$, constant in Q	$\gamma(Q)$ = 1.2−0.7
	n = 2	n = 1
high Γ	$\gamma \simeq 1.5$, constant in Q	$\gamma(Q)$ = 1.8−1.3
	n = 1	n = 0.7

[a] For hydrophilic SiNP samples, upon compression we observe a transition from Brownian diffusion to the arrested state ruled by repulsive interactions as described in the text. For hydrophobic SiNP samples, the dynamics is that of a gel network ruled by attractive interactions, with the localization length of its rearrangements lowered upon compression.

At low compression, before the formation of the dense gel phase, the presence of hydrophobic SiNP leads to an increase of γ from $\simeq$1 up to 1.8 while n decrease from $\simeq$1 to 0.7. In the γ−n plane, this corresponds to a shift of the data—upon compression—along a steep trend indicated by the black arrow. In the case of hydrophilic nanoparticles, the transition from diffusive motion to the arrested state is represented as a curve that starts at γ_0 = 1 and n = 2 (diffusive motion) and reaches, at high surface concentration, roughly the same region of the γ_0−n plane; notably, in this case γ is found to be constant along Q,[13] a remarkable difference from the data reported in Figures 6 and 7. Analogously, γ constant over Q was observed also in aged ferrofluids of hydrophilic nanoparticles.[40] Therefore, the two arrested states found for SiNP of different hydrophilicity are clearly distinguishable.

The ability to discriminate between different dynamical regimes requires an high accuracy in the determination of the relevant features from the analysis of the correlation functions, over a large range of scattering vector. This work demonstrates the unique capabilities of GI-XPCS combined with DFM in providing a complete characterization of the micro/nanoscopic dynamics of interfacial systems, exploiting both the superior spatial resolution of XPCS and the wider field of view of DFM. The combined used of GI-XPCS and DFM give access to a wide range of Q, over 2 orders of magnitude; this leads to a better accuracy in the evaluation of the Q-dependence of the relaxation time, as shown in Figure 5.

Through this, we gave a new insight into the difference between the arrested states obtained by mixing phospholipids with nanoparticles of different hydrophilicity. This has relevant implications for drug delivery systems in which SiNP are currently exploited to tune the release properties, for instance, explaining the mechanism by which drug release rate is increased in lipid−hydrophilic SiNP microparticles[9] and how hydrophobic nanoparticles in nanoemulsions help to protect drugs from gastric fluids while still allowing a gradual, slow release.[6]

■ ASSOCIATED CONTENT

Ⓢ Supporting Information

The Supporting Information is available free of charge on the ACS Publications website at DOI: 10.1021/acs.langmuir.6b00813.

Packing fraction of LC domains; Q dependence of the contrast; Figures S1 and S2 (PDF)

■ AUTHOR INFORMATION

Corresponding Author

*E-mail luigi.cristofolini@unipr.it (L.C.).

Notes

The authors declare no competing financial interest.

ACKNOWLEDGMENTS

We acknowledge COST Actions CM1101 and MP1106 for financial support, Dr. Emilio Macaluso for his help with DFM and epifluorescence microscopy measurements, Dr. Yuriy Chushkin (ESRF) for support and help during GI-XPCS experiments, Karim Lhoste (ESRF) for technical assistance during GI-XPCS experiments, and the ESRF for the provision of beamtime.

REFERENCES

(1) Merino, S.; Martín, C.; Kostarelos, K.; Prato, M.; Vázquez, E. Nanocomposite Hydrogels: 3D Polymer-Nanoparticle Synergies for On-Demand Drug Delivery. *ACS Nano* **2015**, *9*, 4686−4697.

(2) Ashley, C. E.; Carnes, E. C.; Phillips, G. K.; Padilla, D.; Durfee, P. N.; Brown, P. A.; Hanna, T. N.; Liu, J.; Phillips, B.; Carter, M. B.; Carroll, N. J.; Jiang, X.; Dunphy, D. R.; Willman, C. L.; Petsev, D. N.; Evans, D. G.; Parikh, A. N.; Chackerian, B.; Wharton, W.; Peabody, D. S.; Brinker, C. J. The targeted delivery of multicomponent cargos to cancer cells by nanoporous particle-supported lipid bilayers. *Nat. Mater.* **2011**, *10*, 389−397.

(3) Vallet-Regí, M.; Balas, F.; Arcos, D. Mesoporous Materials for Drug Delivery. *Angew. Chem., Int. Ed.* **2007**, *46*, 7548−7558.

(4) Pérez-Esteve, É; Fuentes, A.; Coll, C.; Acosta, C.; Bernardos, A.; Amorós, P.; Marcos, M. D.; Sancenón, F.; Martínez-Máñez, R.; Barat, J. M. Modulation of folic acid bioaccessibility by encapsulation in pH-responsive gated mesoporous silica particles. *Microporous Mesoporous Mater.* **2015**, *202*, 124−132.

(5) Liong, M.; Lu, J.; Kovochich, M.; Xia, T.; Ruehm, S. G.; Nel, A. E.; Tamanoi, F.; Zink, J. I. Multifunctional inorganic nanoparticles for imaging, targeting, and drug delivery. *ACS Nano* **2008**, *2*, 889−96.

(6) Weerapol, Y.; Limmatvapirat, S.; Nunthanid, J.; Sriamornsak, P. Self-Nanoemulsifying Drug Delivery System of Nifedipine: Impact of Hydrophilic-Lipophilic Balance and Molecular Structure of Mixed Surfactants. *AAPS PharmSciTech* **2014**, *15*, 456−464.

(7) Bhatt, A. B.; Barnes, T. J.; Prestidge, C. A. Silica nanoparticle stabilization of liquid crystalline lipid dispersions: impact on enzymatic digestion and drug solubilization. *Curr. Drug Delivery* **2015**, *12*, 47−55.

(8) Salonen, A.; Muller, F.; Glatter, O. Internally self-assembled submicrometer emulsions stabilized by spherical nanocolloids: finding the free nanoparticles in the aqueous continuous phase. *Langmuir* **2010**, *26*, 7981−7.

(9) Albertini, B.; Passerini, N.; Gonzalez-Rodriguez, M. L.; Perissutti, B.; Rodriguez, L. Effect of Aerosil on the properties of lipid controlled release microparticles. *J. Controlled Release* **2004**, *100*, 233−246.

(10) Li, Y.; Chen, X.; Gu, N. Computational Investigation of Interaction between Nanoparticles and Membranes: Hydrophobic/Hydrophilic Effect. *J. Phys. Chem. B* **2008**, *112*, 16647−16653.

(11) Beddoes, C. M.; Case, C. P.; Briscoe, W. H. Understanding nanoparticle cellular entry: A physicochemical perspective. *Adv. Colloid Interface Sci.* **2015**, *218*, 48−68.

(12) Bulpett, J. M.; Snow, T.; Quignon, B.; Beddoes, C. M.; Tang, T.-Y. D.; Mann, S.; Shebanova, O.; Pizzey, C. L.; Terrill, N. J.; Davis, S. A.; Briscoe, W. H. Hydrophobic nanoparticles promote lamellar to inverted hexagonal transition in phospholipid mesophases. *Soft Matter* **2015**, *11*, 8789−8800.

(13) Orsi, D.; Guzmán, E.; Liggieri, L.; Ravera, F.; Ruta, B.; Chushkin, Y.; Rimoldi, T.; Cristofolini, L. 2D dynamical arrest transition in a mixed nanoparticle-phospholipid layer studied in real and momentum spaces. *Sci. Rep.* **2015**, *5*, 17930.

(14) Ponchut, C.; Rigal, J. M.; Clément, J.; Papillon, E.; Homs, A.; Petitdemange, S. MAXIPIX, a fast readout photon-counting X-ray area detector for synchrotron applications. *J. Instrum.* **2011**, *6*, C01069−C01069.

(15) Giavazzi, F.; Cerbino, R. Digital Fourier microscopy for soft matter dynamics. *J. Opt.* **2014**, *16*, 083001.

(16) Abràmoff, M. D.; Magalhães, P. J.; Ram, S. J. Image processing with imageJ. *Biophotonics Int.* **2004**, *11*, 36−41.

(17) Mohwald, H. Phospholipid and Phospholipid-Protein Monolayers at the Air/Water Interface. *Annu. Rev. Phys. Chem.* **1990**, *41*, 441−476.

(18) Klopfer, K.; Vanderlick, T. Isotherms of Dipalmitoylphosphatidylcholine (DPPC) Monolayers: Features Revealed and Features Obscured. *J. Colloid Interface Sci.* **1996**, *182*, 220−229.

(19) Orsi, D.; Vezzani, A.; Burioni, R.; Pucci, A.; Ruggeri, G.; Cristofolini, L. Statistical properties and morphology of a 2D gel network at the air/water interface. *Colloids Surf., A* **2014**, *441*, 912−918.

(20) Orsi, D.; Baldi, G.; Cicuta, P.; Cristofolini, L. On the relation between hierarchical morphology and mechanical properties of a colloidal 2D gel system. *Colloids Surf., A* **2012**, *413*, 71−77.

(21) Luzzati, V.; Reiss-Husson, F.; Rivas, E.; Gulik-Krzywicki, T. Structure and polymorphism in lipid-water systems, and their possible biological implications. *Ann. N. Y. Acad. Sci.* **1966**, *137*, 409−413.

(22) Bergström, L. In *Colloidal Particles at Liquid Interfaces*; Binks, B. P., Horozov, T. S., Eds.; Cambridge University Press: 2006; pp 77−107.

(23) Grübel, G.; Madsen, A.; Robert, A. In *Soft-Matter Characterization*; Borsali, R., Pecora, R., Eds.; Springer: 2008; Chapter 18, pp 935−995.

(24) Berne, B.; Pecora, R. *Dynamic Light Scattering*; Dover: New York, 1976.

(25) Orsi, D.; Cristofolini, L.; Fontana, M.; Pontecorvo, E.; Caronna, C.; Fluerasu, A.; Zontone, F.; Madsen, A. Slow dynamics in an azopolymer molecular layer studied by x-ray photon correlation spectroscopy. *Phys. Rev. E* **2010**, *82*, 031804.

(26) Leheny, R. L. XPCS: Nanoscale motion and rheology. *Curr. Opin. Colloid Interface Sci.* **2012**, *17*, 3−12.

(27) Herzig, E. M.; Robert, A.; van't Zand, D. D.; Cipelletti, L.; Pusey, P. N.; Clegg, P. S. Dynamics of a colloid-stabilized cream. *Phys. Rev. E* **2009**, *79*, 011405.

(28) Angelini, R.; Zulian, L.; Fluerasu, A.; Madsen, A.; Ruocco, G.; Ruzicka, B. Dichotomic aging behaviour in a colloidal glass. *Soft Matter* **2013**, *9*, 10955.

(29) Angelini, R.; Zaccarelli, E.; de Melo Marques, F. A.; Sztucki, M.; Fluerasu, A.; Ruocco, G.; Ruzicka, B. Glass-glass transition during aging of a colloidal clay. *Nat. Commun.* **2014**, *5*, 4049.

(30) Ruta, B.; Czakkel, O.; Chushkin, Y.; Pignon, F.; Nervo, R.; Zontone, F.; Rinaudo, M. Silica nanoparticles as tracers of the gelation dynamics of a natural biopolymer physical gel. *Soft Matter* **2014**, *10*, 4547−4554.

(31) Fluerasu, A.; Moussaïd, A.; Madsen, A.; Schofield, A. Slow dynamics and aging in colloidal gels studied by x-ray photon correlation spectroscopy. *Phys. Rev. E* **2007**, *76*, 010401.

(32) Guzmán, E.; Santini, E.; Ferrari, M.; Liggieri, L.; Ravera, F. Interfacial Properties of Mixed DPPC-Hydrophobic Fumed Silica Nanoparticle Layers. *J. Phys. Chem. C* **2015**, *119*, 21024−21034.

(33) Orsi, D.; Ruta, B.; Chushkin, Y.; Pucci, A.; Ruggeri, G.; Baldi, G.; Rimoldi, T.; Cristofolini, L. Controlling the dynamics of a bidimensional gel above and below its percolation transition. *Phys. Rev. E* **2014**, *89*, 042308.

(34) Bouchaud, J.-P.; Pitard, E. Anomalous dynamical light scattering in soft glassy gels. *Eur. Phys. J. E: Soft Matter Biol. Phys.* **2001**, *6*, 231−236.

(35) Duri, A.; Cipelletti, L. Length scale dependence of dynamical heterogeneity in a colloidal fractal gel. *Europhys. Lett.* **2006**, *76*, 972−978.

(36) Cipelletti, L.; Ramos, L.; Manley, S.; Pitard, E.; Weitz, D. A.; Pashkovski, E. E.; Johansson, M. Universal non-diffusive slow dynamics in aging soft matter. *Faraday Discuss.* **2003**, *123*, 237−251.

(37) Garbin, V.; Crocker, J. C.; Stebe, K. J. Nanoparticles at fluid interfaces: Exploiting capping ligands to control adsorption, stability and dynamics. *J. Colloid Interface Sci.* **2012**, *387*, 1−11.

DOI: 10.1021/acs.langmuir.6b00813
Langmuir 2016, 32, 4868−4876

(38) Ferrero, E. E.; Martens, K.; Barrat, J.-L. Relaxation in Yield Stress Systems through Elastically Interacting Activated Events. *Phys. Rev. Lett.* **2014**, *113*, 248301.

(39) Orsi, D.; Cristofolini, L.; Baldi, G.; Madsen, A. Heterogeneous and anisotropic dynamics of a 2D Gel. *Phys. Rev. Lett.* **2012**, *108*, 105701.

(40) Robert, A.; Wandersman, E.; Dubois, E.; Dupuis, V.; Perzynski, R. Glassy dynamics and aging in a dense ferrofluid. *EPL (Europhysics Letters)* **2006**, *75*, 764.